A Harmonic Optimized Deadbeat Predictive Control Method for Switched Reluctance Machine

Shoujun Song, *Senior Member, IEEE*, Chenyi Yang, Haoyu Yin, Qiyuan Cheng, Chong Bao, Ruiqing Ma, and Weiguo Liu, *Senior Member, IEEE*

***Abstract*—In this article, a deadbeat predictive control (DPC) method with low measurement effort and the capability to effectively suppress torque ripple is proposed for switched reluctance machine (SRM). First, to enhance prediction model accuracy, a flux-linkage model based on second-order Bézier curves combined with full-position interval interpolation is proposed. This method only requires determining three parameters—aligned-position incremental inductance, unaligned-position incremental inductance, and unaligned-position saturation inductance to accurately describe flux-linkage characteristics. Next, Varignon's principle is applied to analyze the mechanism by which phase current harmonics influence torque. On this basis, the beetle antennae search algorithm, which enables rapid optimization, is used to optimize the current waveform, resulting in a novel harmonic-optimized current profile. The developed enhanced DPC methodology incorporating pulsewidth modulation demonstrates significant torque ripple reduction under diverse operating conditions, minimal offline measurement requirements, and high estimation accuracy, thus providing an efficient and practical solution for achieving high-performance SRM control in industrial applications.**

***Index Terms*—Bézier curve, current profile, dead-beat predictive current control, switched reluctance machine (SRM), torque ripple.**

I. Introduction

THE electric aircraft technology has gained considerable attention and is rapidly developing to mitigate the environmental impact of air transportation and move toward more sustainable modes [1]. As one of the core technologies of multielectric engine technology, high-power starter/generator technology demands strict volume and weight specifications [2]. There is a trend toward adopting built-in starter/generators and integrating the starter/generator into the internal high-pressure shaft of the engine. The operating environment temperature during operation can reach 300°C−400°C [3]. Considering factors, such as power density, speed, and temperature, the switched reluctance machine (SRM) exhibits unique advantages in multiphase machine performance [4].

Many methods are employed to suppress the torque ripple of SRMs, thereby improving machine reliability. Existing torque ripple suppression strategies are primarily categorized into two types: current modulation strategies and torque control strategies [5]. Among current waveform optimization strategies, current chopping control (CCC) offers straightforward implementation but suffers from limited control frequency. This limitation hinders accurate current tracking, introduces delays, and restricts its application in high-demand scenarios. Given the critical need for precise current tracking, extensive research has been conducted [6], [7], [8]. SRM current control strategies mainly include deadbeat predictive current control [9], [10], model predictive control [11], [12], and related techniques. For example, Song et al. [13] applied model prediction and deadbeat control to the commutation and single-phase conduction processes of SRMs based on four-quadrant operation. Combined with pulsewidth modulation (PWM) modulation, this approach achieves full-speed-range operation with excellent current tracking. Similarly, Tao and Zhijian [14] introduced an extended state observer to refine reference current values, enhancing tracking accuracy.

In response to problems in traditional current control, some scholars have optimized these strategies and conducted in-depth analysis from the perspective of current profiles. In [15], torque ripple in SRM is addressed by optimizing the rectangular current reference waveform based on inductance–current relationships. In [16], the current profile design is enhanced by leveraging Simulink and finite element analysis, significantly reducing torque ripple in SRM. However, the analysis of the above-mentioned strategies regarding their impact mechanisms is not sufficiently in-depth. In [17], the impact of phase current harmonics in SRM is studied by simulating their injection. This study demonstrates their influence and employs the Lagrange multiplier method for ripple suppression. However, this approach is limited to fixed speeds and loads, posing challenges in practical applications. In [18], by utilizing magnetic motive force, torque ripple in SRM is predicted and suppressed. This approach identifies a strong link between torque ripple, second-order current harmonics, and machine inductance characteristics, and reduces torque ripple by optimizing the switching angle control strategy. In [19], the reference waveform of SRM's phase current is defined as a half-cycle sine wave. By optimizing current harmonic coefficients offline for a fixed torque,

Received 24 April 2025; revised 11 July 2025; accepted 25 August 2025. Date of publication 28 August 2025; date of current version 13 November 2025. This work was supported in part by the National Natural Science Foundation of China under Grant 52277067 and in part by the Shaanxi Provincial Science Foundation for Distinguished Young Scholars under Grant 2023-JC-JQ-44. Recommended for publication by Associate Editor H. Chaoui. *(Corresponding author: Shoujun Song.)*

The authors are with the School of Automation, Northwestern Polytechnical University, Xi'an 710100, China (e-mail: sunnyway@nwpu.edu.cn; 202120-2330@mail.nwpu.edu.cn; yinhaoyu@mail.nwpu.edu.cn; cqy@mail.nwpu.edu.cn; baochong1997@mail.nwpu.edu.cn; marq@nwpu.edu.cn; lwglll@nwpu.edu.cn).

Color versions of one or more figures in this article are available at https://doi.org/10.1109/TPEL.2025.3603616.

Digital Object Identifier 10.1109/TPEL.2025.3603616

effective suppression of torque ripple is achieved using genetic and differential algorithms. In [20], the position angle and torque error are utilized as fuzzy inputs to adaptively determine current harmonic coefficients for each segment. These coefficients are injected into the phase current reference waveform, modifying the output torque to suppress torque ripple across a broad range of speeds and loads

An accurate prediction model is also an essential part of achieving efficient deadbeat control. The existing prediction models mainly include the lookup table method and the analytical method [21], [22]. In [23], the flux-linkage characteristics are measured at four positions, and a polynomial Fourier series model is developed to reduce torque ripple. In [24], a third order Bézier curve is used to model flux-linkage characteristics, but it has issues with complex coefficient calculation. In [25], a quasilinear flux linkage model with Varignon's parallelogram principle is proposed, requiring only four data points for torque estimation. In [26], it is applied for torque control, achieving good results. In [27], the flux linkage and torque are estimated by combining Hermite interpolation and position interpolation functions, suppressing torque ripple with a torque sharing function model for predictive control.

To co-optimize the existing problems, this article conducts the following work:

1) An analytical model for flux linkage and torque characteristics of switched reluctance motors is developed, prioritizing computational efficiency and prediction accuracy.
2) Analysis of the influence of phase current harmonics on the torque of SRM.
3) Based on the influence mechanism of phase-current harmonics on torque, a harmonic-optimized current waveform design method is proposed.

Finally, a simple harmonic-optimized dead-beat predictive control (DPC) method for switched reluctance motors is completed.

The rest of this article is organized as follows. Section II introduces the proposed prediction model, Section III presents the harmonic-optimized current profile design method, and Section IV verifies the control performance of the proposed method under various operating conditions through experiments. Finally, Section V concludes this article.

II. Prediction Model Improvement

This article proposes a second-order Bézier curve-based estimation method. The method requires only the flux-linkage characteristics at the rotor aligned and unaligned positions, which requires less data and is more effective, and its modeling process is as follows.

At the unaligned rotor position, the flux-linkage $\psi_{ph}(\theta_{\mathrm{u}}, i_{ph})$ can be written as follows:

$$\psi_{ph}(\theta_{\mathrm{u}}, i_{ph}) = L_u i_{ph} \tag{1}$$

where L_u is the slope of the flux linkage in the nonaligned position.

At the aligned rotor position, there are three situations divided by the phase current i_{s0}, i_{s1}, i_{s2}. The determine process of i_{s0}, i_{s1}, i_{s2} can be found in [25].

1) If $i_{ph} \le i_{s1}$, the flux-linkage can be expressed as follows:

$$\psi(\theta_{\mathrm{a}}, i_{ph}) = L_a i_{ph} \tag{2}$$

where L_a is the slope of the unsaturated flux linkage at the aligned position.

2) If $i_{s1} \le i_{ph} \le i_{s2}$ the flux-linkage curve can be expressed as Bézier curve. The basic model of the second-order Bézier curve can be expressed as follows:

$$B(t) = (1-t^2)P_0 + 2t(1-t)P_1 + t^2 P_2 \quad t \in [0,1] \tag{3}$$

where P_k is the control point, $k = 0, 1, 2$. In this article, P_0 is the curve start point, P_2 is the curve end point, and P_1 is used as an intermediate point to determine the behavior between the start point and the end point. Therefore, this part of the flux-linkage can be expressed as follows:

$$i_{ph}(t) = (1-t^2)i_{s0} + 2t(1-t)i_{s1} + t^2 i_{s2} \tag{4}$$

$$\psi(t) = (1-t^2)\psi_{s0} + 2t(1-t)\psi_{s1} + t^2\psi_{s2} \tag{5}$$

$$\psi_{s0} = L_a i_{s0} \tag{6}$$

$$\psi_{s1} = L_a i_{s1} \tag{7}$$

$$\psi_{s2} = L_{as} i_{s2} + f \tag{8}$$

$$\psi(\theta_a, i_{ph}) = \left[1 - t(i_{ph})^2\right]\psi_{s0} + 2t(i_{ph})\left[1 - t(i_{ph})\right]\psi_{s1} + t(i_{ph})^2\psi_{s2}. \tag{9}$$

From (4)–(9), when the i_{ph}(t) is fixed, t is then fixed. it can be seen that at a fixed position, the flux-linkage is only the function of the current i_{ph}. All other parameters are fixed, and for ease of understanding.

3) If $i_{ph} > i_{s2}$, the flux-linkage can be expressed as follows:

$$\psi_{ph}(\theta_{\mathrm{a}}, i_{ph}) = L_{as} i_{ph} + f \tag{10}$$

where L_{as} and f are the slope and intercept of the saturated flux linkage at the aligned position, respectively.

In conclusion, at the aligned position, the flux-linkage can be written as (11) shown at the bottom of this page.

In order to estimate the characteristics of the flux-linkage between aligned and unaligned position, a nonlinear position interpolation function [5] is therefore introduced, as follows:

$$f(\theta) = \begin{cases} \frac{2N_r{}^3\theta^3}{\pi^3} - \frac{3N_r{}^2\theta^2}{\pi^2} + 1 & \theta \in \left[0, \frac{\pi}{8}\right] \\ f\left(\frac{\pi}{4} - \theta\right) & \theta \in \left[\frac{\pi}{8}, \frac{\pi}{4}\right]. \end{cases} \tag{12}$$

$$\psi(\theta_{\mathrm{a}}, i_{ph}) = \begin{cases} L_a i_{ph} & i_{ph} \le i_{s1} \\ \left[1 - t(i_{ph})^2\right]\psi_{s0} + 2t(i_{ph})\left[1 - t(i_{ph})\right]\psi_{s1} + t(i_{ph})^2\psi_{s2} & i_{s1} \le i_{ph} \le i_{s2} \\ L_{az} i_{ph} + f & i_{ph} > i_{s2}. \end{cases} \tag{11}$$

Therefore, the flux-linkage characteristics at any position can be expressed as follows:

$$\psi(\theta, i_{ph}) = \psi(\theta_u, i_{ph}) + [\psi(\theta_a, i_{ph}) - \psi(\theta_u, i_{ph})]\, f(\theta). \tag{13}$$

Assuming a constant current between two consecutive points, the instantaneous torque at any point on the closed loop curve can be expressed as follows:

$$T_e = \left[\frac{\partial W'}{\partial \theta}\right]_{i=\text{ constant}}. \tag{14}$$

Considering (7)–(13), the instantaneous torque can be written as follows:

$$\begin{aligned} T_e = \; & \left[f_1(i_{s0}, i_{s1}, i_{s2}, \psi_{s0}, \psi_{s1}, \psi_{s2}, L_u) {i_{ph}}^2 \right. \\ & + f_3(i_{s0}, i_{s1}, i_{s2}, \psi_{s0}, \psi_{s1}, \psi_{s2}) i_{ph} \\ & \left. + f_2(i_{s0}, i_{s1}, i_{s2}, \psi_{s0}, \psi_{s1}, \psi_{s2})(A i_{ph} + B)^{3/2}\right] f'(\theta). \end{aligned} \tag{15}$$

Among them, in the practical application process f_1, f_2, f_3, A, and B are known data, shown at the top of this page. And the obtained expressions are only functions of the current, which do not require complex calculations, such as integration, differentiation, and exponential operations, and the amount of operations is less compared to traditional methods (16)–(20) shown at the bottom of this page

In [28], the method of measuring the flux-linkage characteristics using torque balance is used to determine the actual flux-linkage characteristics at two positions of 0° and 22.5°. This method does not require prior information about the machine, a rotor position fixing device, or a rotor position sensor. It only needs to utilize the characteristic that the torque of the SRM is zero at the aligned position and the nonaligned position. By applying different pulse voltages to each phase, the flux-linkage characteristics can be confirmed.

The proposed method for predicting the characteristics of SRM is compared with the traditional method [27], as shown in Fig. 1, and it can be seen that the proposed prediction model is closer to the experimental data and the implementation process is relatively simple. The root-mean-square error of the flux-linkage is 0.0020 Wb.

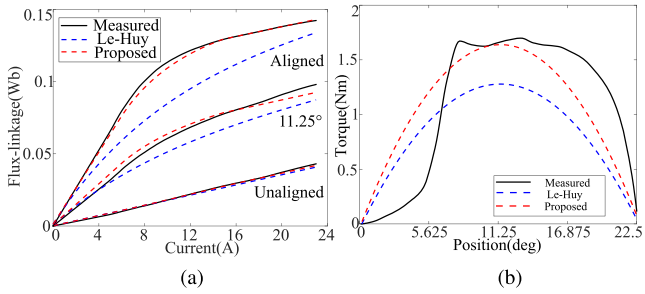

Fig. 1. Electromagnetic characteristics comparison. (a) Flux-linkage characteristics. (b) Torque characteristics at 9 A.

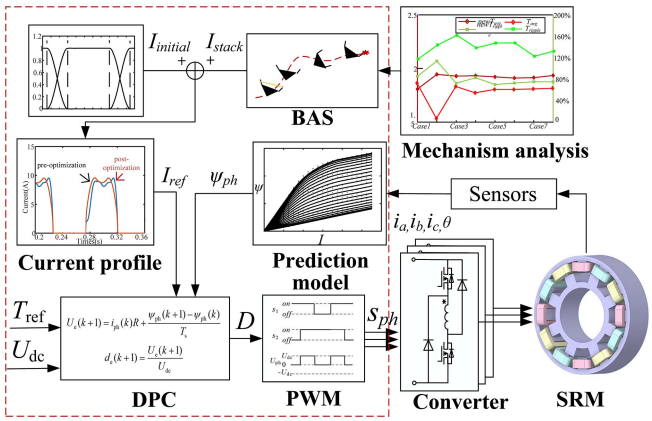

Fig. 2. Control block diagram of proposed method.

III. Proposed DPC

As shown in Fig. 2, the basic process is as follows. On the basis of the initial current profile, the current profile is optimized using the beetle antennae search (BAS) algorithm combined with the harmonic influence mechanism of the phase current, and this optimized profile serves as the current reference for the next moment; then the new prediction model obtains the flux-linkage parameters at both current and next moments, which are combined with the given duty cycle signals and discretized voltage equations. Finally, an improved PWM modulation method generates control signals for the switching devices in each phase of the asymmetric half-bridge, thus achieving effective suppression of SRM torque ripple.

$$A = 4\left(i_{s2} - i_{s0} - 2i_{s1}\right) \tag{16}$$

$$B = 4{i_{s1}}^2 - 4i_{s0}\left(i_{s2} - i_{s0} - 2i_{s1}\right) \tag{17}$$

$$f_1(i_{s0}, i_{s1}, i_{s2}, \psi_{s0}, \psi_{s1}, \psi_{s2}, L_u) = \frac{1}{2}\left(\frac{\psi_{s2} - \psi_{s0} - 2\psi_{s1}}{i_{s2} - i_{s0} - 2i_{s1}} - L_u\right) \tag{18}$$

$$f_2(i_{s0}, i_{s1}, i_{s2}, \psi_{s0}, \psi_{s1}, \psi_{s2}) = \frac{\psi_{s1}(i_{s2} - i_{s0} - 2i_{s1})^2 - 2i_{s1}\left(i_{s2} - i_{s0} - 2i_{s1}\right)\left(\psi_{s2} - \psi_{s0} - 2\psi\right)_{s1}}{6(i_{s2} - i_{s0} - 2i_{s1})^3} \tag{19}$$

$$f_3(i_{s0}, i_{s1}, i_{s2}, \psi_{s0}, \psi_{s1}, \psi_{s2}) = \frac{3{i_{s1}}^2\left(\psi_{s2} - \psi_{s0} - 2\psi_{s1}\right) - i_{s0}\left(i_{s2} - i_{s0} - 2i_{s1}\right)\left(\psi_{s2} - \psi_{s0} - 2\psi_{s1}\right)}{6\left(i_{s2} - i_{s0} - 2i_{s1}\right)^2} + \psi_{s0}. \tag{20}$$

TABLE I
SPECIFIC PARAMETERS OF THE EMPLOYED SRM

Symbol	Parameter	Value
ω_n	Rated speed	1500 rpm
T_n	Rated torque	3 Nm
N_p	Number of phases	3
N_s	Number of stator poles	12
N_r	Number of rotor poles	8
β_s	Stator pole arc	15°
β_r	Rotor pole arc	17°

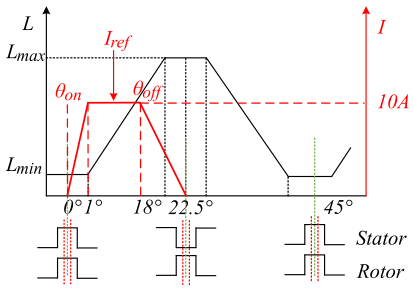

Fig. 3. Constructed reference current.

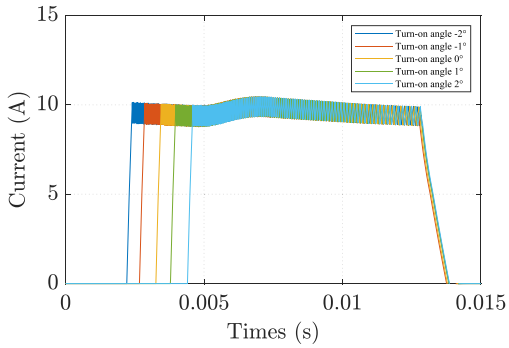

Fig. 4. Current waveforms under different turn-ON angles.

A. Torque Impact Analysis of Phase Current Harmonics

Some scholars have used a rectangular waveform as the reference current waveform [17]. However, considering the different rates of current change at different positions, an asymmetric trapezoid is more appropriate as the reference current. In this article, the amplitudes at key positions of the reference current are determined based on the structural parameters of the SRM [7], and the parameters of the SRM are shown in Table I.

Taking the one-phase change process as an example, the phase current peaks at a small inductance value, then enters single-phase conduction, and finally drops to zero before the inductance value starts to decrease in this region, and the final reference current is shown in Fig. 3.

As shown in Fig. 4, under five different operating conditions, the single-phase current waveforms of the machine are basically the same. This indicates that the construction of the above-mentioned reference current is effective.

TABLE II
REFERENCE CURRENT CRITICAL POSITION PARAMETERS

Reference current	0°	1°	18°	22.5°
Asymmetric trapezoidal				
Rectangular	10 A	10 A	10 A	0 A

The currents of three phases vary periodically, as shown in (21). Only the Fourier decomposition of the A-phase current is analyzed in the subsequent analysis

$$\begin{cases} i_A(\theta) = I_0 + \sum_{m=1}^{\infty} I_m \sin(m\theta + \beta_m) \\ i_B(\theta) = I_0 + \sum_{m=1}^{\infty} I_m \sin(m\theta + \beta_m + 120°) \\ i_C(\theta) = I_0 + \sum_{m=1}^{\infty} I_m \sin(m\theta + \beta_m + 240°) \end{cases} \tag{21}$$

where m is the current harmonic order, I_m is the m-order current harmonic amplitude, and β_m is the electrical angle, while the effective calculation of the torque is realized by adopting the instantaneous torque resolving strategy based on Varignon's parallelogram principle [25], whose basic calculation equations are as follows:

$$T_e = \frac{\left[\Delta L_s \left(i_r^2 - i_s^* i_r\right) + \Delta L_u i_s^* i_r + \Delta \psi_s \left(i_r - i_s^*\right)\right]}{2\Delta\theta}. \tag{22}$$

According to the above-mentioned formula, the instantaneous torque can be expressed as follows: (23) shown at the bottom of the next page.

It can be seen that the torque is mainly composed of three parts, the first part consists of the dc component of the phase current and its square term, the second part consists of the harmonic component of the phase current and its square term, and the third part consists of the interaction of the current harmonic terms.

In this article, two reference currents are constructed based on waveform simulations under 600 rpm and 2 Nm load conditions. The first is an asymmetric trapezoidal reference current, while the second is an ideal rectangular reference current. The amplitudes of both reference currents at different positions are presented in Table II. Corresponding harmonic amplitudes of the phase currents are shown in Fig. 5.

It can be seen that the asymmetric trapezoidal reference current will contain the fifth harmonic and integer multiples of the fifth harmonic compared to the rectangular reference current in the ideal case. Meanwhile, according to the decomposition results, the first eight orders of the phase current harmonics are the main components, and the ninth and higher harmonic amplitude components account for a smaller proportion. Therefore, in order to reduce the complexity of calculation, this article mainly analyzes the impact mechanism of the first eight order phase current harmonics on the output torque of SRM.

In order to verify the influence of different order current harmonics on the torque, this article constructs nine different order harmonics superimposed current waveforms for the two

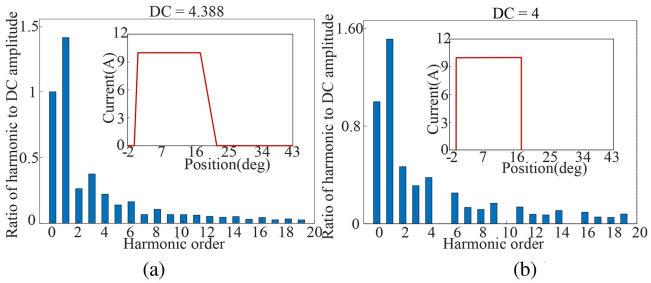

Fig. 5. Reference current Fourier decomposition results. (a) Asymmetric trapezoidal reference. (b) Rectangular reference.

TABLE III
TORQUE CALCULATION RESULTS FOR DIFFERENT CASES

Stacked order	Proposed		Rectangular	
	Average	Ripple	Average	Ripple
Reference waveform	1.9301	0.6954	1.8135	1.1787
Dc+ first order	1.8708	0.8542	1.5313	1.4416
Dc+ first two orders	1.9450	1.1382	1.8296	1.6204
Dc+ first three orders	1.9291	0.7262	1.7707	1.3879
Dc+ first four orders	1.9331	0.8286	1.9014	1.4778
Dc+ first five orders	1.9218	0.7017	1.8014	1.4778
Dc+ first six orders	1.9112	0.7287	1.8068	1.2304
Dc+ first seven orders	1.9150	0.7531	1.8127	1.3206
Dc+ first eight orders	1.9351	0.7523	1.8135	1.2977

reference current as the basis of analysis, and adopts the following evaluation indexes:

$$\text{Ripple} = \frac{T_{\max} - T_{\min}}{T_{\text{avg}}} \times 100\% \tag{24}$$

where Ripple, $T_{\max}$, $T_{\min}$, T_{avg} represent the ripple, maximum, minimum, and average values of torque, respectively.

According to (24), the torque ripple and average torque for different cases are obtained, as shown in Table III. It can be seen that the difference in average torque between the two reference current under the same situation is small, and the difference in torque ripple is relatively obvious.

Based on the data in the above-mentioned table, it can be known that the average torque generated by each order of current harmonics of the asymmetric trapezoidal reference current as a percentage of the total flat torque is shown in Fig. 6. It can be seen that the average torque is mainly composed of the dc component and the first-order current harmonics, and the second-order

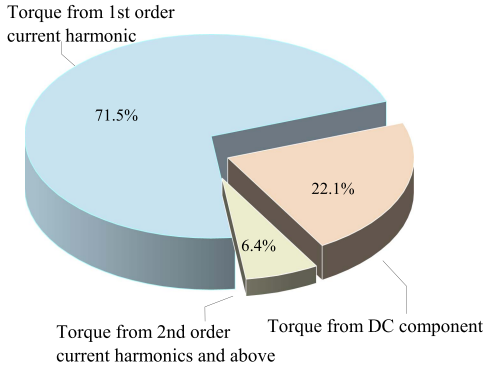

Fig. 6. Percentage of torque generated by each order of current harmonics.

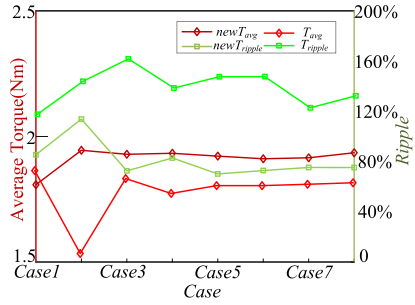

Fig. 7. Trend of torque change in different cases.

and higher current harmonics contribute less to the average torque.

Subsequently, to verify the effect of current harmonic orders on torque ripple magnitude, we analyzed trends in average torque and torque ripple progression with increasing harmonic order, as shown in Fig. 7. As superimposed harmonic orders increase, average torque gradually rises before stabilizing, while torque ripple initially increases then subsides. The first eight harmonic orders exert significant influence on torque ripple, particularly with the third and fifth orders demonstrating measurable suppression effects. Higher order harmonics exhibit diminishing torque ripple fine-tuning capabilities beyond the eighth order, with progressively attenuated adjustment effects at elevated orders.

B. Harmonic-Optimized Current Profile Design

On the basis of obtaining the reference torque, this article introduces the BAS algorithm [29] to improve the traditional current profile which has a long computation period and a long time to find the optimal result.

$$\begin{aligned} T_e = {} & \frac{\Delta L_s {I_0}^2 + (\Delta L_s {i_s}^* - {i_s}^* + \Delta\psi_s) I_0 - \Delta\psi_s {i_s}^*}{2\Delta\theta} \\ & + \frac{(\Delta L_s {i_s}^* - {i_s}^* + \Delta\psi_s) \sum_{m=1}^{\infty} I_m \sin(m\theta + \beta_m) + \Delta L_s \sum_{m=1}^{\infty} {I^2}_m \sin^2(m\theta + \beta_m)}{2\Delta\theta} \\ & + \frac{2\Delta L_s \sum_{m=1}^{\infty} \sum_{n=1}^{\infty} I_m I_n \sin(m\theta + \beta_m) \sin(n\theta + \beta_n)}{2\Delta\theta} m \neq n. \end{aligned} \tag{23}$$

The basic principle of the BAS algorithm is as follows.

Define the solution objective as an n-dimensional vector, the left and right tentacles as x_l and x_r. The coordinates of the tenebrae itself as x_0, and the distance between the two tentacles as d_0. At the initial moment, the left tentacle of the tenebrae is pointing in an arbitrary direction with respect to the right tentacle, as determined by the random vector.

First, normalize its initial direction

$$\text{dir} = \frac{\text{dir}}{\text{normal}(\text{dir})}. \tag{25}$$

The vector of the left tentacle to the right tentacle can be expressed as follows:

$$x_l - x_r = d_0 \times \text{dir}. \tag{26}$$

Also, the left and right tentacles can be determined based on the position of the beetle

$$x_l = x_0 + \frac{d_0 \times \text{dir}}{2} \tag{27}$$

$$x_r = x_0 - \frac{d_0 \times \text{dir}}{2}. \tag{28}$$

Defining the optimization objective function as $f_{\text{slove}}(\text{x})$, the objective function values calculated by the left and right tentacles of the beetle during the optimization search process can be expressed as $f_{\text{leftslove}}(\text{x})$ and $f_{\text{rightslove}}(\text{x})$. Therefore, the magnitude of the objective function values obtained by the left and right tentacles can be compared to realize the movement of the position of the beetle.

For example, if $f_{\text{leftslove}}(\text{x}) < f_{\text{rightslove}}(\text{x})$, the left tentacle gets a smaller value of the objective function, and then the beetle moves one step in the direction of the left tentacle

$$x_0 = x_0 + \text{step} \times \text{normal}(x_l - x_r). \tag{29}$$

Conversely, if the right tentacle obtains a smaller value for the objective function, the beetle moves one step in the direction of the right tentacle

$$x_0 = x_0 - \text{step} \times \text{normal}(x_l - x_r). \tag{30}$$

The two equations can be harmonized as follows:

$$\text{x}_0 = \text{x}_0 - \text{step} \times \text{dir} \times \text{sgn}(f_{\text{leftslove}} - f_{\text{rightslove}}). \tag{31}$$

As can be seen, the core code of BAS has only four lines, and its construction model is simple, requires few parameters, is easy to implement. Therefore, the basic flowchart and pseudocode of the harmonic optimization current profile design method in this section is shown in Fig. 8.

1) *Initial current profile determination:* An initial current profile reference can be obtained based on the established prediction model combined with the inverse interpolation method.
2) *Optimize parameter initialization:* The amplitude and phase of the superimposed current harmonics are set as optimization variables and the merit of the torque ripple is used as an evaluation function.
3) *BAS algorithm optimization:* The writing of the BAS algorithm and the optimization analysis of the parameters are mainly implemented in the workspace, while Simulink iterates to obtain the evaluation function values.

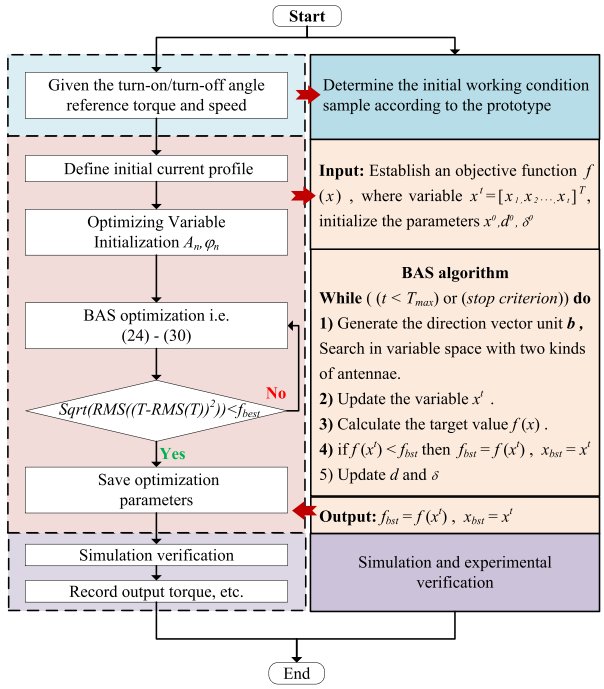

Fig. 8. Current profile optimization flowchart.

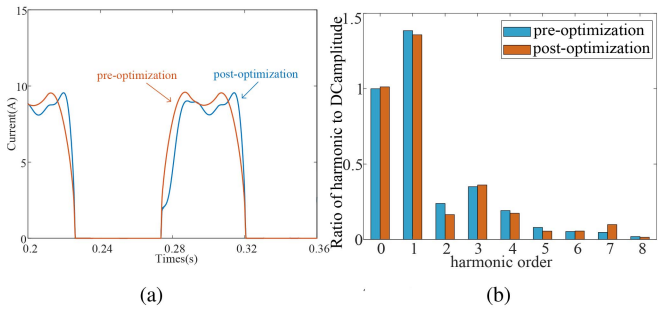

Fig. 9. Results of current profile optimization. (a) Comparison of current profile. (b) Comparison of harmonic amplitude percentage.

Based on the above-mentioned process, the current profile optimization process for the SRM at 800 rpm with constant load of 1.5 Nm is described as follows.

Among them, Fig. 9(a) shows the current profiles before and after optimization. After harmonic superposition, the reference current increases in regions with higher inductance change rates while decreasing in regions with lower inductance change rates. This adjustment not only compensates for torque deficiency during phase transitions but also avoids high-current demands in low-inductance-change regions, thereby effectively reducing torque ripple while maintaining efficiency. Simultaneously, the percentage distribution of current harmonic amplitudes shifts, as shown in Fig. 9(b).

C. Other Improvements

To address excessive current fluctuations in traditional PWM modulation, we introduce an improved PWM method [13].

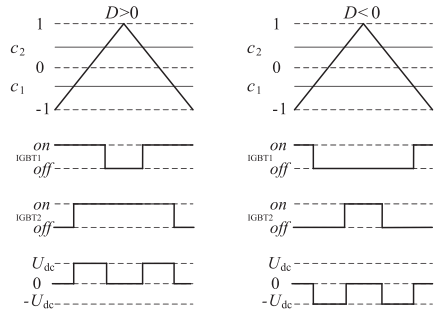

Fig. 10. Introduction of PWM modulation method.

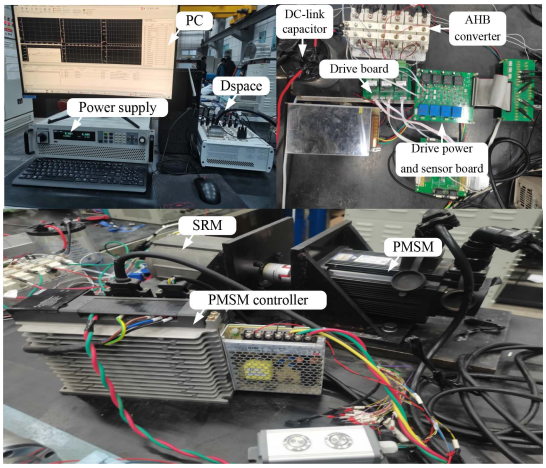

Fig. 11. Experimental platform.

This approach modifies control signal generation for switching devices IGBT1 and IGBT2 as follows. IGBT1 activates when the carrier wave exceeds the high-level threshold of duty cycle D, and deactivates otherwise; IGBT2 deactivates when the carrier wave falls below the negative low-level threshold of duty cycle D, and activates otherwise. This expanded voltage regulation range consequently reduces torque ripple. Fig. 10 illustrates the conduction logic schematic.

IV. Experimental Verification

This article implements a dSPACE-based SRM rapid prototyping platform shown in Fig. 11 to validate the proposed torque ripple suppression method, prioritizing functional verification over practical cost and computational constraints. The experimental setup comprises three key elements: mechanical components including the experimental prototype and load machine; electrical systems featuring dSPACE controller, asymmetric half-bridge power converter, driver board, signal conditioning board, and sensors; and supporting laboratory infrastructure. Operating at 20 kHz control frequency with 96 V supply voltage, real-time monitoring of speed, torque, and current waveforms is achieved through ControlDesk software on the host computer.

In order to quantitatively evaluate the optimization effect, this article mainly analyzes the torque and efficiency from two perspectives, and first defines them.

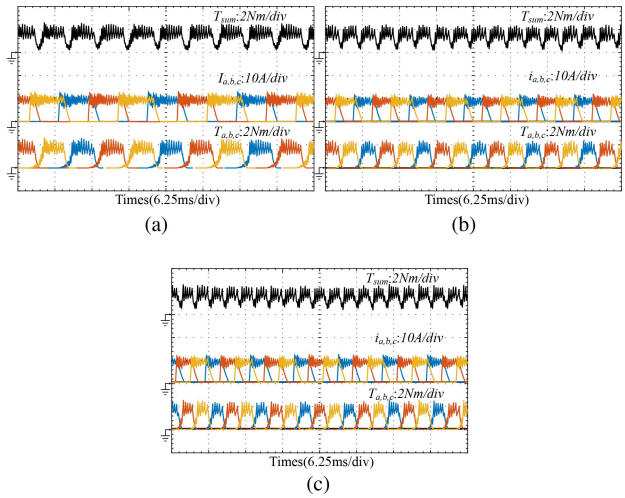

Fig. 12. Experimental results of steady state of CCC. (a) 500 rpm with 1.5 Nm load. (b) 800 rpm with 1.5 Nm load. (c) 1000 rpm with 1.5 Nm load

The torque ripple T_{ripple} is defined as follows:

$$T_{\text{ripple}} = \sqrt{\frac{1}{\theta_1 - \theta_2} \int_{\theta_1}^{\theta_2} (T(\theta) - T_{\text{avg}})^2 d\theta} \tag{32}$$

where θ_1 and θ_2 are the initial position and the end position in a rotor position cycle, respectively.

The average torque T_{avg} is defined as follows:

$$T_{\text{avg}} = \frac{1}{\theta_1 - \theta_2} \int_{\theta_1}^{\theta_2} T(\theta) d\theta. \tag{33}$$

The system efficiency η is defined as follows:

$$\eta = \frac{T_{\text{avg}} \omega}{U_{\text{dc}} I_{\text{dc}}} \times 100\% \tag{34}$$

where ω, U_{bus}, I_{bus} represent the machine speed, bus voltage, and bus current, respectively.

A. Steady-State Performance Verification

In order to effectively validate the proposed control method, this article first carries out a comparison of the steady state performance of the CCC method, the traditional DPC method and the proposed control method. In the experimental verification of the CCC for steady state conditions, the switching angles are set to 0° and 18°, the given load size is 1.5 Nm, and the given speeds are 500, 800, 1000, and 1200 rpm, respectively. The experimental tests have obtained the waveforms of torque, phase currents, and phase torque for different operating conditions.

First, the given load is 1.5 Nm, and the given speeds are 500, 800, and 1000 rpm, respectively. the experimental waveforms of the CCC are shown in Fig. 12. It can be seen that under the steady state, with the increase of speed, the number of current chopping gradually becomes less, which leads to the existence of large torque ripple.

The experimental results of the DPC are shown in Fig. 13, and under the DPC method allocates the currents in each phase independently, so the torque ripple can be effectively suppressed.

TABLE IV
EXPERIMENTAL RESULTS OF THE THREE METHODS AT DIFFERENT ROTATIONAL SPEEDS UNDER 1.5 NM

	CCC			DPC			Proposed method		
Speed	500	800	1000	500	800	1000	500	800	1000
Average	1.464	1.523	1.544	1.486	1.521	1.535	1.514	1.553	1.564
Torque ripple	0.53	0.47	0.45	0.18	0.16	0.15	0.08	0.06	0.08
Efficiency	49.5%	60.6%	65.5%	54.06%	63.1%	66.9%	54.5%	63.8%	66.4%

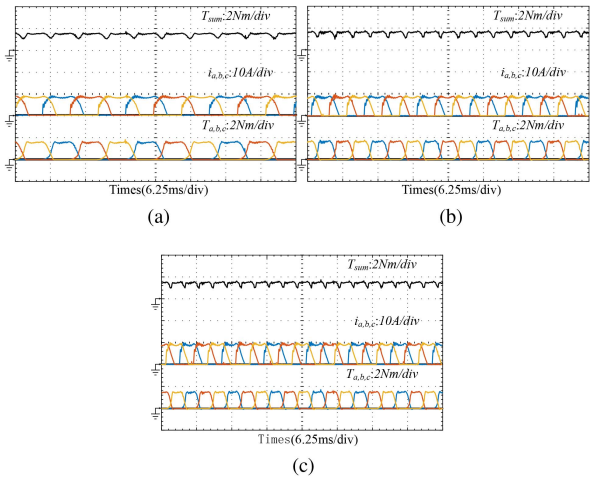

Fig. 13. Experimental results of steady state of DPC. (a) 500 rpm with 1.5 Nm load. (b) 800 rpm with 1.5 Nm load. (c) 1000 rpm with 1.5 Nm load.

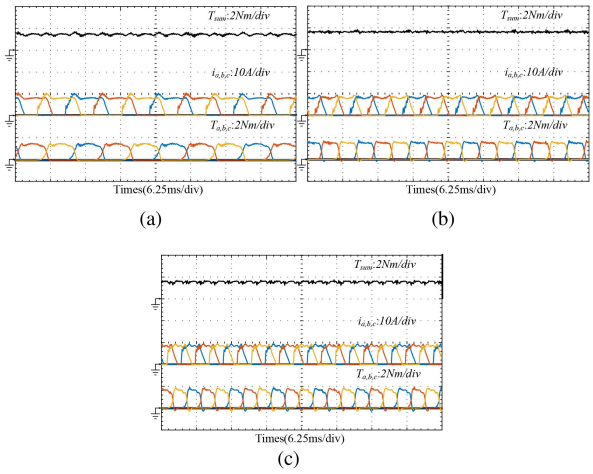

Fig. 14. Experimental results of steady state of proposed method. (a) 500 rpm with 1.5 Nm load. (b) 800 rpm with 1.5 Nm load. (c) 1000 rpm with 1.5 Nm load.

However, the torque ripple still exists because the current profile is ideal, and the asymmetric current change caused by the nonlinear characteristic is not considered, thus there is a certain amount of torque ripple.

The control method proposed in this article effectively solves the above-mentioned problems of the traditional control strategy in which the current profile is more ideal and the accuracy of the prediction model is poor, and the experimentally obtained steady state waveforms are shown in Fig. 14.

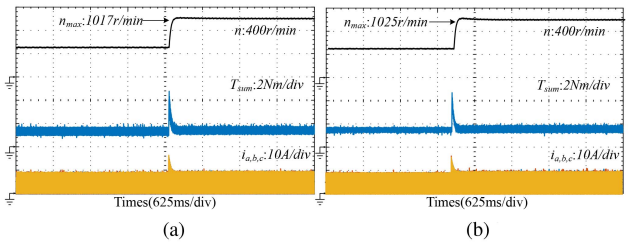

Fig. 15. Results of the speed changing from 500 to 1000 rpm at 1.5 Nm. (a) DPC. (b) Proposed method.

From the experimental results and data in Table IV, it can be seen that the proposed method with 1.5 Nm load at different speed bands has the best torque ripple suppression effect compared to the other two control strategies, the torque is smoother, and it is able to reduce the torque ripple of the DPC strategy by about 50% in all operating conditions, and the efficiency does not decrease in all operating conditions, so its overall performance is better.

The torque ripple, average torque, and efficiency of the machine under different operating conditions are also obtained to verify the generalizability of the proposed method, as shown in Table V. It can be seen that the proposed method has a better torque ripple suppression effect in steady state operation under different working conditions, and the efficiency of the proposed method is improved with the increase of the system speed and load torque, which is due to the fact that at this time, the ratio of the system output power to the total input power is gradually increasing, while the loss power is basically unchanged.

B. Dynamic Performance Verification

In order to effectively verify the dynamic performance of the system, this section experimentally compares and analyzes the dynamic performance of the DPC and the proposed method under two working conditions, variable load at constant speed and variable speed at constant load, respectively. First, the system is experimentally verified for the working condition with 1.5 Nm load where the speed is abruptly changed from a given 500 to 1000 rpm, as shown in Fig. 15. According to the experimental results, it can be seen that the dynamic response time of the two method is about 0.25 s during the sudden change of speed from 500 to 1000 rpm, and there is no phenomenon, such as oscillation overshooting, which is a good dynamic response capability. In the response process, the proposed method can

TABLE V
EXPERIMENTAL RESULTS OF DIFFERENT WORKING CONDITIONS OF THE PROPOSED METHOD

	500 rpm			800 rpm			1000 rpm		
Carried load	1	1.5	2	1	1.5	2	1	1.5	2
Average	1.085	1.514	1.963	1.151	1.553	2.011	1.17	1.564	2.032
Torque ripple	0.08	0.05	0.12	0.09	0.06	0.12	0.10	0.08	0.12
Efficiency	52.5 %	54.5%	52.3%	63.5 %	63.8%	63.5%	67.9%	66.4%	66.2%

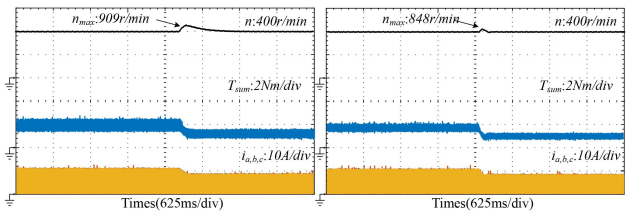

Fig. 16. Result of the load changing from 2 to 1 Nm at 800 rpm. (a) DPC. (b) Proposed method.

effectively suppress the torque ripple in the whole process under the premise of ensuring good dynamic response capability.

According to Fig. 16, it can be seen that during the sudden change of load torque from 2 to 1 Nm at a constant speed of 800 rpm for both control methods, the proposed method has less speed ripple, which is able to better adapt to the process of the sudden change of its load. The phase currents of the two are basically the same during the process, and the proposed method is able to maintain a good suppression of the load torque before and after the load variation.

V. CONCLUSION

This article proposes a direct power control method characterized by simplicity, ease of implementation, and effective torque ripple suppression. Experimental validation across varying speeds and torques confirms the method effectively suppresses torque ripple while maintaining near-constant efficiency. The principal contributions are summarized as follows.

1) A prediction modeling method based on the Bézier curve is proposed, which requires only the flux-linkage characteristics of aligned and nonaligned positions, and establishes the model with high accuracy.
2) The mechanism of the influence of phase current harmonics on torque of SRM is analyzed and obtained.
3) Based on the mechanism, a harmonic phase current profile design method is proposed to effectively suppress the torque ripple by using the BAS algorithm.

Overall, these methods provide a versatile foundation for advancing SRM technology, with promising extensions to emerging domains, such as electric vehicles and renewable energy systems.

REFERENCES

[1] Y. Liang, G. R. C. Mouli, and P. Bauer, "Charging technology for electric aircraft: State of the art, trends, and challenges," *IEEE Trans. Transp. Electrific.*, vol. 10, no. 3, pp. 6761–6788, Sep. 2024.

[2] J. Wei, H. Xu, B. Zhou, Z. Zhang, and C. Gerada, "An integrated method for three-phase AC excitation and high-frequency voltage signal injection for sensorless starting of aircraft starter/generator," *IEEE Trans. Ind. Electron*, vol. 66, no. 7, pp. 5611–5622, Jul. 2019.

[3] G. Sun, S. Song, J. Jiang, L. Ge, and W. Liu, "Characteristics testing and torque control of aero-engine shaft-line-embedded switched reluctance starter/generator," *IEEE Trans. Ind. Appl.*, vol. 59, no. 6, pp. 7295–7305, Nov./Dec. 2023.

[4] L. Ge et al., "Advanced technology of switched reluctance machines in more electric aircraft: A review," *IEEE Trans. Power Electron.*, vol. 40, no. 1, pp. 195–216, Jan. 2025.

[5] G. Fang, F. P. Scalcon, D. Xiao, R. P. Vieira, H. A. Gründling, and A. Emadi, "Advanced control of switched reluctance motors (SRMs): A review on current regulation, torque control and vibration suppression," *IEEE Open J. Ind. Electron. Soc.*, vol. 2, pp. 280–301, 2021.

[6] F. P. Scalcon, G. Fang, R. P. Vieira, H. A. Gründling, and A. Emadi, "Discrete-time super-twisting sliding mode current controller with fixed switching frequency for switched reluctance motors," *IEEE Trans. Power Electron.*, vol. 37, no. 3, pp. 3321–3333, Mar. 2022, doi: 10.1109/TPEL.2021.3116096.

[7] T. Husain, A. Elrayyah, Y. Sozer, and I. Husain, "Unified control for switched reluctance motors for wide speed operation," *IEEE Trans. Ind. Electron*, vol. 66, no. 5, pp. 3401–3411, May 2019.

[8] S. Zhang, O. Wallscheid, and M. Porrmann, "Machine learning for the control and monitoring of electric machine drives: Advances and trends," *IEEE Open J. Ind. Appl.*, vol. 4, pp. 188–214, 2023.

[9] F. Yunsheng, L. Yue, and L. Di, "Predictive current control of switched reluctance motor based on extended observer," in *Proc. 6th Int. Conf. Automat., Control Robot. Eng.*, Dalian, China, 2021, pp. 150–156.

[10] A. Biswas, S. Dhale, S. Khzym, and A. Emadi, "Detailed implementation of hardware-in-the-loop validation of an advanced energy management controller for power-split HEVs," in *Proc. Int. Conf. Comput., Commun., Intell. Syst.*, Greater Noida, India, 2022, pp. 229–236.

[11] D. F. Valencia, R. Tarvirdilu-Asl, C. Garcia, J. Rodriguez, and A. Emadi, "Vision, challenges, and future trends of model predictive control in switched reluctance motor drives," *IEEE Access*, vol. 9, pp. 69926–69937, 2021.

[12] M. Pereira and R. E. Araújo, "Model-free finite-set predictive current control with optimal cycle time for a switched reluctance motor," *IEEE Trans. Ind. Electron*, vol. 70, no. 8, pp. 8355–8364, Aug. 2023.

[13] S. Song, J. Liu, Y. Zhao, L. Ge, R. Ma, and W. Liu, "High-dynamic four-quadrant speed adjustment of switched reluctance machine with torque predictive control," *IEEE Trans. Ind. Electron*, vol. 69, no. 8, pp. 7733–7743, Aug. 2022.

[14] C. Tao and Q. Zhijian, "The current predictive control method of switched reluctance motor based on commutation interval subdivision," in *Proc. 2023 IEEE PELS Students Young Professionals Symp.*, Shanghai, China, 2023, pp. 1–5.

[15] F. Peng, J. Ye, and A. Emadi, "A digital PWM current controller for switched reluctance motor drives," *IEEE Trans. Power Electron.*, vol. 31, no. 10, pp. 7087–7098, Oct. 2016.

[16] K. Hu and J. Ye, "Offline current profiling schemes for torque ripple reduction in mutually coupled switched reluctance machines using a three-phase voltage source converter," in *Proc. IEEE Energy Convers. Congr. Expo.*, Detroit, MI, USA, 2022, pp. 1–7.

[17] Z. Q. Zhu, B. Lee, L. Huang, and W. Chu, "Contribution of current harmonics to average torque and torque ripple in switched reluctance machines," *IEEE Trans. Magn*, vol. 53, no. 3, Mar. 2017, Art. no. 8100909.

[18] Z. Shuguang, L. Mingtian, H. Shenglong, and W. Hao, "Torque ripple reduction of switched reluctance motor by optimising switch angle based on analytical modelling," *IET Electric Power Appl.*, vol. 14, 1488–1495, 2020.

[19] N. T. Shaked and R. Rabinovici, "New procedures for minimizing the torque ripple in switched reluctance motors by optimizing the phase-current profile," *IEEE Trans. Magn.*, vol. 41, no. 3, pp. 1184–1192, Mar. 2005.
[20] D. F. Valencia, R. Tarvirdilu-Asl, C. Garcia, J. Rodriguez, and A. Emadi, "A review of predictive control techniques for switched reluctance machine drives. part i: Fundamentals and current control," *IEEE Trans. Energy Convers.*, vol. 36, no. 2, pp. 1313–1322, Jun. 2021.
[21] L. Ge, Z. Fan, N. Du, J. Huang, D. Xiao, and S. Song, "Model predictive torque and force control for switched reluctance machines based on online optimal sharing function," *IEEE Trans. Power Electron.*, vol. 38, no. 10, pp. 12359–12364, Oct. 2023.
[22] L. Ge, J. Zhong, J. Huang, and S. Song, "Model predictive torque control of switched reluctance machine based on torque-balanced measurement and flux-based torque estimation," in *Proc. 24th Int. Conf. Elect. Mach. Syst.*, Gyeongju, Korea, Republic of, 2021, pp. 867–872.
[23] L. Ge, J. Zhong, J. Huang, N. Jiao, S. Song, and R. W. De Doncker, "A novel model predictive torque control of SRMs with low measurement effort," *IEEE Trans. Ind. Electron*, vol. 70, no. 4, pp. 3561–3570, Apr. 2023.
[24] C. S. Matwankar, S. Pramanick, and B. Singh, "Flux-linkage characterization and rotor position estimation of switched reluctance motor using bézier curves," in *Proc. IEEE 2nd Int. Conf. Smart Technol. Power, Energy Control*, Bilaspur, Chhattisgarh, India, 2021, pp. 1–6.
[25] A. Stuikys, B. Zaghari, and J. K. Sykulski, "Instantaneous electromagnetic torque waveform calculations for switched reluctance machines exploiting vector analysis," *IEEE Trans. Magn.*, vol. 57, no. 1, Jan. 2021, Art. no. 8100111.
[26] C. Yang, C. Bao, S. Song, Q. Cheng, J. Zhong, and C. Liu, "High dynamic direct instantaneous torque control of switched reluctance machine based on magnetic co-energy torque estimation," in *Proc. 25th Int. Conf. Elect. Mach. Syst.*, Chiang Mai, Thailand, 2022, pp. 1–6.
[27] S. Song, R. Hei, R. Ma, and W. Liu, "Model predictive control of switched reluctance starter/generator with torque sharing and compensation," *IEEE Trans. Transp. Electrific.*, vol. 6, no. 4, pp. 1519–1527, Dec. 2020.
[28] L. Ge, I. Ralev, A. Klein-Hessling, S. Song, and R. W. De Doncker, "A simple reluctance calibration strategy to obtain the flux-linkage characteristics of switched reluctance machines," *IEEE Trans. Power Electron.*, vol. 35, no. 3, pp. 2787–2798, Mar. 2020.
[29] M. Lin, Q. Li, F. Wang, and D. Chen, "An improved beetle antennae search algorithm and its application on economic load distribution of power system," *IEEE Access*, vol. 8, pp. 99624–99632, Dec. 2020.

Shoujun Song (Senior Member, IEEE) received the B.S. and M.S. degrees from Northwestern Polytechnical University, Xi'an, China, in 2003 and 2006, respectively, and the Dr.-Ing. degree from the Technical University of Berlin, Berlin, Germany, in 2009, all in electrical engineering.

He is currently a Professor with the School of Automation, Northwestern Polytechnical University. His research interests include electric machines and drives in more electric aircraft with an emphasis on switched reluctance machines and permanent magnet machines.

Dr. Song was the recipient of the 2018, 2019, and 2023 Best Paper Awards from the International Conference on Electrical Machines and Systems. He is an Associate Editor for IEEE TRANSACTIONS ON INDUSTRIAL ELECTRONICS and IEEE TRANSACTIONS ON TRANSPORTATION ELECTRIFICATION.

Chenyi Yang received the B.S. and M.S. degrees in electrical engineering from Northwestern Polytechnical University, Xi'an, China, in 2021 and 2024, respectively. He is currently working toward the Ph.D. degree in electrical engineering with the Harbin Institute of Technology, Harbin, China.

His research interests include advanced control strategies for reluctance machines and permanent magnet synchronous machines, and the design of high-speed permanent magnet machines.

Dr. Yang was the Recipient of Best Paper Award in the 26th International Conference on Electrical Machines and Systems.

Haoyu Yin was born in China, in 2002. He received the B.S. degree in electrical engineering from Northeast Forestry University, Harbin, China, in 2024. He is currently working toward the M.S. degree in electrical engineering with Northwestern Polytechnical University, Xi'an, China.

His research interests include advanced control and parameter identification of reluctance motors.

Qiyuan Cheng was born in China, in 1999. He received the B.S. degree in electrical engineering from Northwestern Polytechnical University, Xi'an, China, in 2021, where he is currently working toward the the Ph.D. degree in electrical engineering.

His research interests include electrical machines and drives with emphasis on the design and control of switched reluctance machines.

Chong Bao received the B.S. degree in electrical engineering from Liaoning University, Shenyang, China, in 2018. He is currently working toward the Ph.D. degree in electrical engineering with Northwestern Polytechnical University, Xi'an, China.

His research interests include advanced control of reluctance machines and permanent magnet synchronous machines.

Ruiqing Ma received the B.S., M.S., and Ph.D. degrees in electrical engineering from Northwestern Polytechnical University, Xi'an, China, in 1985, 1988, and 2007, respectively.

He is currently a Professor with the School of Automation, Northwestern Polytechnical University. His research interests include permanent magnet electric machines, power converters, and renewable energy systems.

Weiguo Liu (Senior Member, IEEE) received the B.S. degree in electrical machine engineering from the Huazhong University of Science and Technology, Wuhan, China, in 1982, and the M.S. degree in electrical engineering and the Ph.D. degree in control theory and control engineering from Northwestern Polytechnical University, Xi'an, China, in 1988 and 1999, respectively.

He is currently a Professor with the School of Automation, Northwestern Polytechnical University. His research interests include brushless dc machines, PM synchronous machines, and induction machines.